Experiments in Fluids (2019) 60:145
https://doi.org/10.1007/s00348-019-2785-3

RESEARCH ARTICLE

Instabilities in micro-contraction flows of semi-dilute CTAB and CPyCl solutions: rheology and flow instabilities

R. M. Matos[1,3] · M. A. Alves[2] · F. T. Pinho[1]

Received: 6 June 2019 / Revised: 26 July 2019 / Accepted: 27 July 2019

Abstract

The flows of two semi-dilute surfactant solutions (CTAB and CPyCl) through several micro contractions/expansions are experimentally investigated, following an extensive rheological characterization in both shear and extensional flows. The shear rheology of the solutions shows strong shear thinning and shear banding, whereas Small Amplitude Oscillatory Shear and Capillary Break-up Extensional Rheometry indicate that they have high shear and extensional elasticities. Flow visualizations and micro-particle image velocimetry measurements show that the surfactant solutions exhibit three established types of flow patterns in contraction flows: Newtonian-like, asymmetric and disordered. Newtonian-like flow occurs at low flow rates and is preceded by a long transient flow in experiments starting from rest, which seems to be related to shear banding and the alignment of wormlike micelles. The asymmetric flow regime occurs at moderate flow rates and is characterized by an asymmetric upstream central jet with two adjacent vortices, features that change non-periodically, but slowly, in time. This flow pattern seems to be related with the high elasticity of the semi-dilute solutions. The disordered flow pattern is similar to the asymmetric flow in terms of broad characteristics, but the flow asymmetry changes with time much faster than in the asymmetric flow regime, resembling a chaotic-like flow. The disordered flow seems to be related with the breakdown of micellar structures. We concluded also that the flows in both the asymmetric and disordered flow regimes are globally stable in terms of flow patterns, but locally unstable in terms of flow characteristics, with power spectra of the velocity fluctuations having slopes that differ from those typically encountered in elastic turbulence.

✉ F. T. Pinho
fpinho@fe.up.pt

R. M. Matos
romeu.martins.matos@gmail.com

[1] CEFT, Departamento de Engenharia Mecânica, Faculdade de Engenharia da Universidade do Porto, Rua Dr. Roberto Frias, 4200-465 Porto, Portugal

[2] CEFT, Departamento de Engenharia Química, Faculdade de Engenharia da Universidade do Porto, Rua Dr. Roberto Frias, 4200-465 Porto, Portugal

[3] Present Address: ENC Energy, Rua dos Terços 575, 4410-236 Canelas, Portugal

Published online: 23 August 2019

Graphic abstract

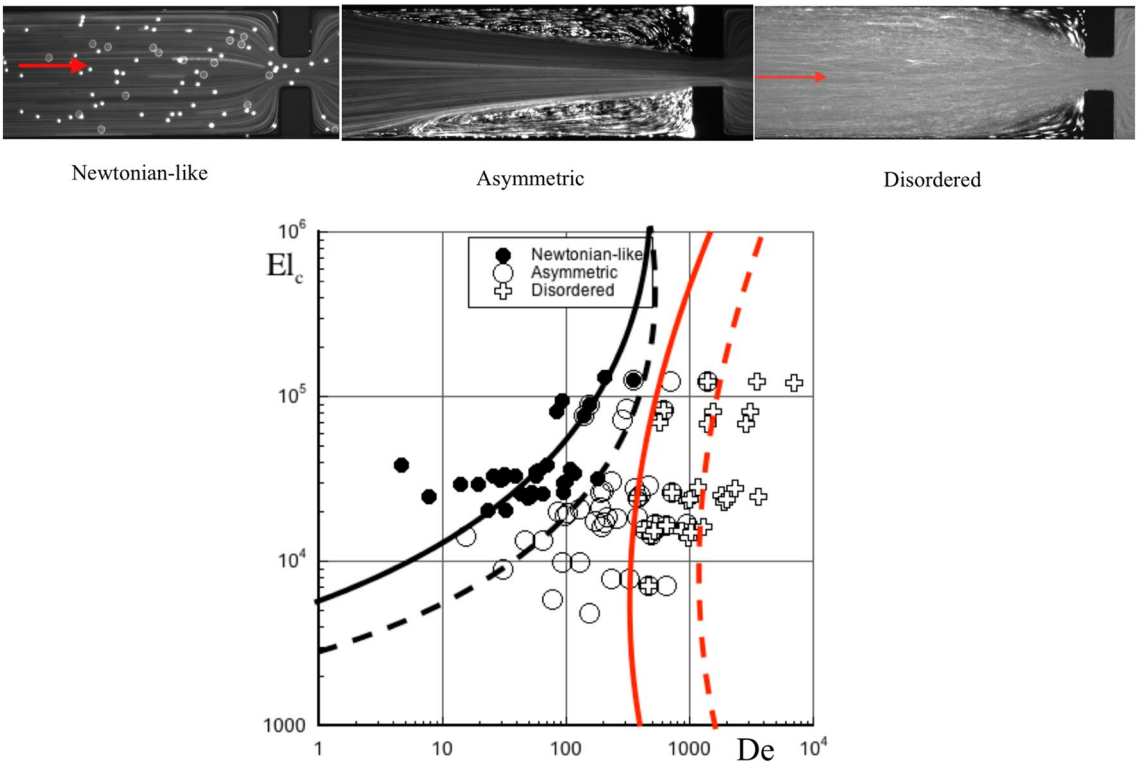

1 Introduction

Surface active agents, commonly known as surfactants, are chemical compounds that lower the surface tension at interfaces, and are widely used in a variety of applications within the food, pharmaceuticals, detergents, environment and construction industries. They are usually used as dispersants, detergents, foaming agents, wetting agents or emulsifiers (Rehage and Hoffmann 1988).

From the late 1960s to the 1980s, it was found that a small addition of surfactants to an otherwise Newtonian solvent led to a severe drag reduction in wall turbulent flows due to the viscoelastic nature of the surfactant solutions (Savins 1967; Povkh et al. 1975; Bewersdorff et al. 1986), but the unusual behavior of these solutions was not limited to turbulent flows and could also be observed under lower Reynolds numbers flow conditions, such as flow though porous media as is found in enhanced oil recovery or hydraulic fracturing (Holmberg et al. 1998), amongst others. The pursuit of understanding and human curiosity led to further investigations on the rheology of these dilute solutions, also because it was difficult to measure their properties, with measurements too close to the limits of the equipment (Berret 2005; Puig et al. 2012).

The advent of microfluidics in which flows usually involve complex fluids and where such phenomena as elastic turbulence has been observed (Groisman and Steinberg 2000) motivated this work, where we focus on the rheology and flow instabilities of two semi-dilute surfactant solutions in microchannels.

The rheology of semi-dilute surfactant solutions in steady shear and in Small Amplitude Oscillatory Shear (SAOS) flows is currently reasonably well documented. However, the extensional behavior is still the subject of many investigations, particularly because the low surface tension of those solutions makes it more difficult to perform Capillary Breakup Extensional Rheometry (CaBER) measurements (Lopez-Diaz et al. 2010; Manero et al. 2010; Puig et al. 2012). The advent of microfluidics has opened the possibility to investigate the extensional behavior as well as flow instabilities of semi-dilute surfactant solutions (Koskie and Tiederman 1991; Hu et al. 1998; Kawaguchi et al. 2002; Zakin and Ge 2010).

Dubash et al. (2012) studied the flow dynamics of two semi-dilute CTAB solutions, and reported three different

types of flow patterns in cross-slot flows: steady symmetric, steady asymmetric and unsteady asymmetric flow. They also found that the transition between those states varied significantly and depended on the combination of several factors such as the Weissenberg number (*Wi*), the Reynolds number (*Re*) and the rheology of the surfactant solutions. Haward and McKinley (2012) also found similar features in cross-slot flows with semi-dilute CPyCl solutions. The present work addresses the fluid dynamics of contraction–expansion flows with semi-dilute CTAB and CPyCl solutions and complements the above mentioned cross-slot flow investigations, providing additional information about the fluid dynamics.

Lutz-Bueno et al. (2015) also investigated the behavior of wormlike micelles in flows through a slit channel using Small-Angle Neutron-Scattering (SANS) experiments. Their measurements were carried out for 10 min and showed the average scattering of the wormlike micelles conformations. In the upstream channel and at the contraction, the data showed the presence of an anisotropic fluid structure, which suggests an alignment of the wormlike micelles in those regions, and an isotropic fluid structure in the downstream flow, usually associated with a random alignment of the wormlike micelles. Their semi-dilute solution exhibited a strong cone-like entry flow with upstream recirculations that are the outcome of its strong extensional elasticity. The large dimensions of the slit channel used by Lutz-Bueno et al. (2015) lead to non-negligible inertial effects on the measured flow conditions. Again, it is an objective of this work to also complement the investigations of Lutz-Bueno et al. (2015), since with our microchannels it is possible to investigate the flow dynamics at high *Wi* without the influence of inertial effects. Additionally, the flow visualizations also allow the study of transient flows, and the analysis of flows through confined contractions–expansions can also foster numerical investigations on flows of semi-dilute surfactant solutions, because it provides experimental information about the behavior of flow characteristics and flow instabilities.

The next section describes the experimental methods and is divided into three subsections about the preparation of the fluids, the rheological devices and methods, and the microchannel setup, respectively. The flow visualizations are reported afterwards, first characterizing the three flow patterns found (Newtonian-like; asymmetric; disordered flow) and this is followed by an analysis of flow transitions through parameter space maps and data from micro-particle image velocimetry (μ-PIV) measurements. Finally, this work ends with a summary of the main findings.

2 Experimental methods

2.1 Fluids

The two semi-dilute solutions of Cetyltrimethylammonium Bromide (CTAB) and Cetylpyridinium Chloride (CPyCl), both with NaSal (Sodium Salicylate) as a co-surfactant, were prepared at molar concentrations of 100 mM of CTAB with 32 mM of NaSal and 100 mM of CPyCl with 60 mM of NaSal, both in deionized water. The solutions were gently mixed for a week using a magnetic stirrer to avoid any agglomeration and this was followed by a 24 h period at rest. The same solutions were previously characterized and studied by Dubash et al. (2012) and Haward et al. (2012). All reagents used were supplied by Sigma Aldrich.

2.2 Rheology

A Physica MCR301 (Anton Paar) rotational rheometer with a CP50-2 truncated cone-plate geometry (2° cone angle, 50 mm diameter) was used to characterize the steady shear viscosity (shear rates up to 100 s^{-1}) and the response of the fluids in SAOS. A solvent trap was used to minimize evaporation and to better control the temperature of the samples. In addition, microchannels were also used to investigate the occurrence of flow instabilities and the steady shear rheology at high shear rates, but the details of the microchannels are described below.

The extensional rheology was measured using a Capillary Break-up Extensional Rheometer (CaBER) (Haake CaBER 1, Thermo Electron), which imposes an uniaxial extensional step deformation on the fluid sample. The final gap was set to allow the monitoring of the time evolution of the filament diameter, but was also large enough to induce the break-up of the liquid sample bridge by capillary forces (Kim et al. 2010). Typically, the final gap used was about three times the diameter of the plates.

2.3 Microchannels

The flows through the microchannels were under controlled flow rate conditions and for that purpose the setup incorporates a syringe pump (neMESYS, Cetoni). In addition, the setup contains a filter, connecting pipes and needles, as shown in Fig. 1a. The syringe pump uses syringes of different volumes, all supplied by Hamilton: 100 µl (1710N ga22S/51mm/pst2), 250 µl (1725N ga22S/51mm/pst2), 500 µl (1750N ga22S/51mm/pst2), 1000 µl (1001LTN ga22/51mm/pst5), 2500 µl (1002LTN ga22/51mm/pst5) and 5000 µl (1005LTN ga22/51mm/pst5).

The outlet is connected to a small container, at atmospheric pressure, to receive the waste fluid.

The microchannels are of three different types: straight channels, used to characterize the steady shear rheology at high shear rates; abrupt contractions–expansions (designated henceforth as abrupt contractions), which were used in μPIV measurements and flow visualizations; and hyperbolic contractions/abrupt expansions (designated as hyperbolic contractions) used only in the flow visualizations.

Figure 2 illustrates schematically the straight microchannels used to characterize the steady rheology of the semi-dilute surfactant solutions, which are approximately 3 mm long with a constant width of approximately 100 μm and two different depths (50 and 100 μm). The pressure drops at the inlet smooth contraction and at the outlet smooth expansion (near points 1 and 2, respectively, in Fig. 2) are small when compared to the pressure drop over the whole length of the thin straight channel. The measurements were carried out after more than 5 min at a constant flow rate, and the measured pressure drop is the time average of the reading over 1 min. This measurement procedure was assessed initially by measuring the viscosity of water, but the estimated measurement error for any tested fluid was between 10 and 15% when compared to the shear viscosity measured in the rotational rheometer.

The straight microchannel measurements used three differential pressure transducers with different operating ranges: 1 psi (model 26PCAFA6D), 5 psi (26PCBFA6D) and 15 psi (26PCCFA6D); all models were supplied by Honeywell. The sensors were calibrated using a high precision manometer for higher pressures and a column of water for lower pressure differences.

In all contraction channels the contraction–expansion is located at the middle of a long straight channel to decrease

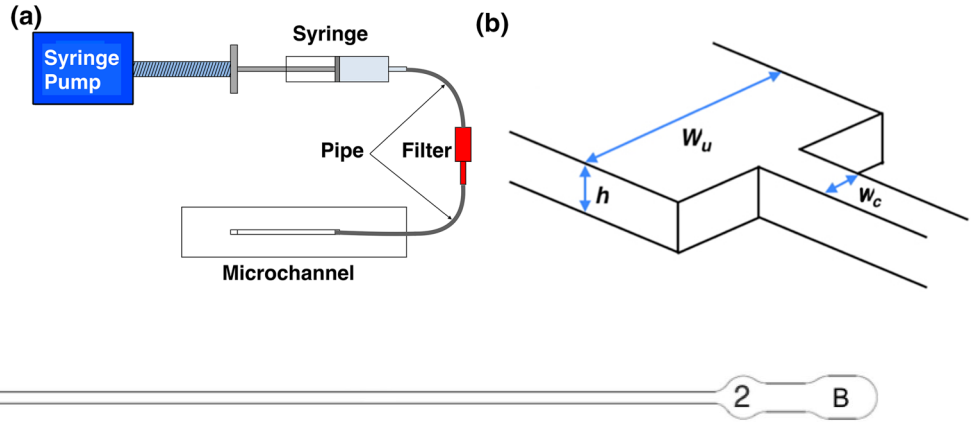

Fig. 1 **a** Illustration of the controlled flow rate setup. **b** Schematic of the contraction with a rectangular cross section

Fig. 2 Schematic of the straight microchannels with two pressure holes (1 and 2), and one entrance (A) and exit (B) ports

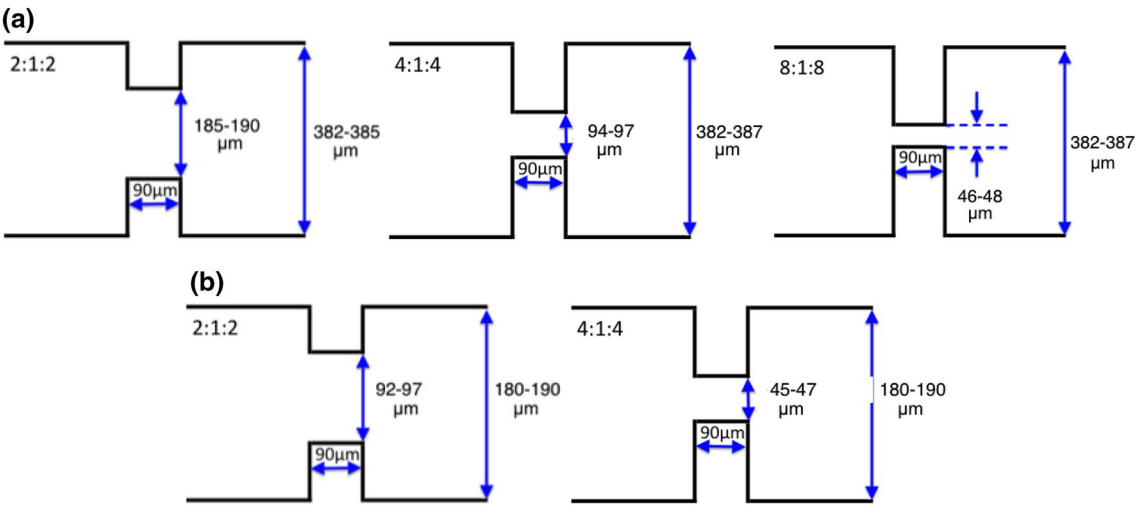

Fig. 3 Microchannels layout and contraction–expansion ratios with the real dimensions indicated. Channel widths: **a** $w_u = 385 \pm 2$ μm. **b** $w_u = 185 \pm 5$ μm

the influence of both the entrance and the exit of the channel on the contraction flow. Figure 3 shows the different types of contraction channels with different nominal contraction–expansion ratios (2:1:2, 4:1:4 and 8:1:8), widths ($w_u = 200$ and 400 µm) and depths ($h = 200$, 100 and 50 µm). However, after the fabrication process, the contraction ratios, as well as the overall dimensions of the channels were slightly different from the design values. At the end, the real dimensions of the channels are those listed in Fig. 3, but for simplicity the geometries are still denoted by their design dimensions.

Figure 4 shows the hyperbolic contractions and the corresponding abrupt contractions. Here, only two different nominal depths were used, $h = 50$ and 100 µm (real measured depths between $h = 45$–48 µm and 89–90 µm, respectively).

2.4 Flow visualizations and microPIV

The system used in the flow visualization experiments includes an inverted fluorescence microscope (DMI 5000 M, Leica Microsystems GmbH) with a filter cube, a 100 W mercury light source and the use of spherical fluorescent tracer particles with average diameter of 1 µm (Invitrogen, Nile red) at a mass concentration around 100 ppm. Tests with the same type of tracer particles were also carried out at other mass concentrations to understand their influence on the flow, as well as on the flow images themselves. For the nominal conditions above, tracer particles were found to have a negligible influence on the flow.

The microscope was equipped with an objective with 10 × magnification and numerical aperture NA = 0.3 in most of the experiments, while the experiments with longer recirculations and jets were carried out with an objective with 5 × magnification and NA = 0.12. All the experiments were carried out at the middle plane of the microchannels.

Two different µPIV setups were used: a fast setup which can acquire pairs of images at high frequencies (up to 10 kHz), and another setup that is restricted to low frequencies (up to 7.4 Hz). The latter is constituted by the same microscope used in the flow visualization experiments, but a double-pulsed 532 nm Nd:YAG laser (Dual Power 65–15, Dantec Dynamics), and a CCD digital camera (Flow Sense 4 M, Dantec Dynamics) were used. On the other hand, the fast µPIV setup uses a different microscope (Olympus IX83), a diode pumped pulsed 526.5 nm Nd:YLF laser (Litron Lasers LDY300) and a high-speed CMOS camera (Phantom Miro M340, Vision Research). In the µPIV measurements, the particle concentration was 400 ppm, and 32 × 32 pixels interrogation windows were used. The time between images was optimized for each channel and flow rate, based on the upstream channel velocity at the central plane. Generally speaking, the time between the images varied from 10 ms for the highest flow rate ($Q = 42.5$ µl/min) in the shallower

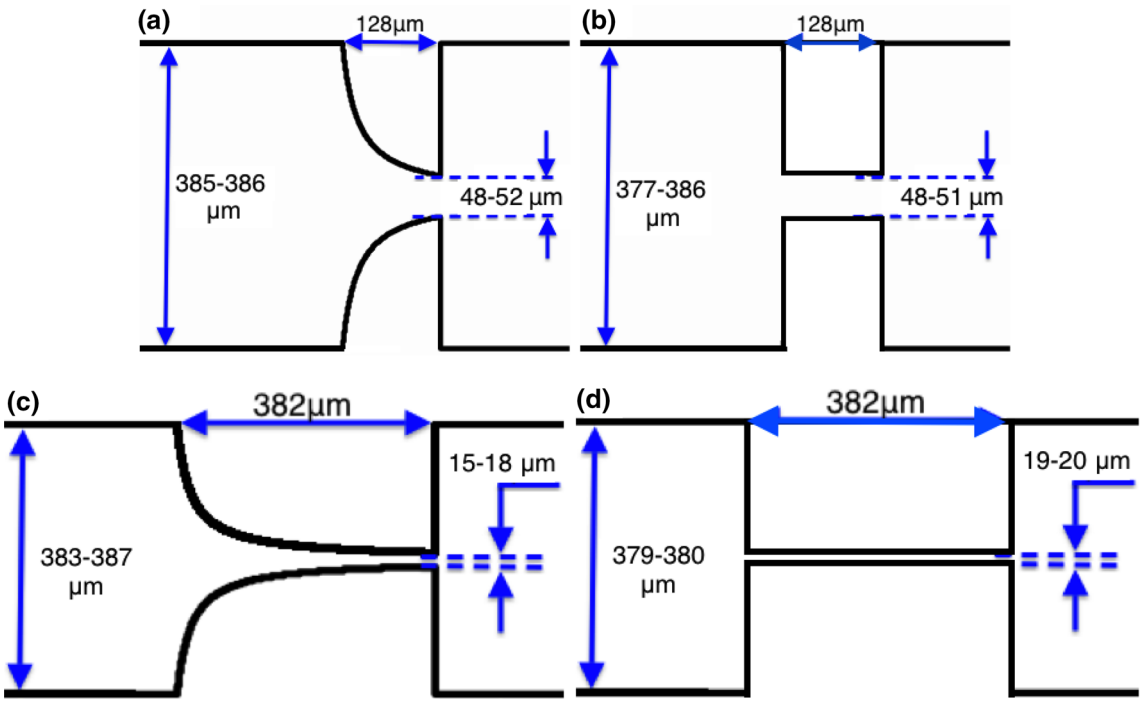

Fig. 4 Microchannels layout and the contractions ratios with the real dimensions indicated. Channel widths: **a** HC1; **b** C1; **c** HC2; **d** C2. *HC* hyperbolic contraction, *C* abrupt contraction

channel ($h \approx 50$ µm) up to 700 ms for the lowest flow rate ($Q = 4.25$ µl/min) in the deeper channel ($h \approx 100$ µm).

3 Results and discussion

3.1 Fluid rheology

The time evolution of the shear stress measured in the rotational rheometer at three different shear rates ($\dot{\gamma} = 1$, 10 and 100 s^{-1}) and of the pressure gradient measured in straight channels for five different flow rates ($Q = 1.37$, 2.95, 6.36, 13.6 and 29.5 µl/min) are plotted in Fig. 5a, b, respectively.

In the rheometer, the time required to achieve steady state conditions is particularly long for the experiments carried out at $\dot{\gamma} = 1$ s^{-1}, of more than 1700 s from the onset of the experiment from the rest state. The experiments also suggest that an acquisition time of 150 s for each data point is a reasonable compromise to describe the steady shear rheology of the semi-dilute solutions over a wide range of shear rates. The evolution with time of the pressure gradient in the microchannel flows (Fig. 5b) also shows the long time required to achieve steady state conditions. Similar behavior was observed with CPyCl solutions.

Figure 6a plots the steady shear viscosity as a function of the shear rate for both surfactant solutions and includes the data obtained in the rotational rheometer and in the straight microchannels.

Qualitatively, the behavior of both semi-dilute solutions is similar. At low shear rates ($\dot{\gamma} < 0.1$ s^{-1}) the steady shear viscosity curves show the Newtonian plateau typical of fluids in a nearly rest state, and it is followed by a strong shear-thinning region corresponding to the constant shear stress plateau (0.1 $s^{-1} < \dot{\gamma} < 100$ s^{-1}), which is a strong indicator of the occurrence of shear banding. The measurements also reveal the presence of a second Newtonian plateau at high shear rates, which is the outcome of the complete alignment of the wormlike micelles (Sood et al. 1999; Berret 2005). For both fluids, the rheometric data suggests the existence of hysteresis.

The constant shear stress plateau on the shear-thinning/shear-banding region is higher for the semi-dilute CPyCl solution, suggesting more entangled and/or longer wormlike micellar microstructures than for the CTAB solution. The CPyCl solution also exhibits less pronounced hysteresis and more consistent data than the CTAB solution, because the CPyCl solution takes less time to achieve steady state flow conditions.

Figure 6a also shows the Carreau–Yasuda model described by Eq. (1) fitted to the data of both semi-dilute solutions

$$\eta = \eta_\infty + (\eta_0 - \eta_\infty)\left[1 + (\Lambda\dot{\gamma})^a\right]^{\frac{n-1}{a}} \quad (1)$$

where η_0 and η_∞ are the shear viscosities at low and high shear rates, respectively, n is the power law slope of the shear stress–shear rate curve in the shear-thinning region in log–log coordinates, Λ is the reciprocal shear rate marking the onset of shear thinning and a is an empirical coefficient that controls the sharpness of the transition from the first Newtonian-like plateau to the shear-thinning region.

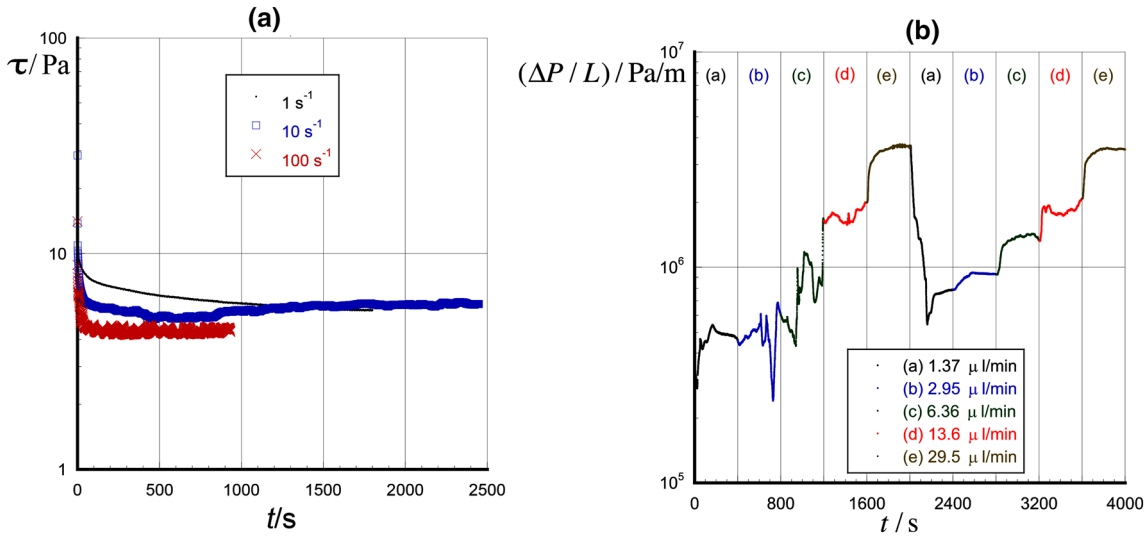

Fig. 5 Time evolution of the shear stress for constant shear rates of $\dot{\gamma} = 1$, 10 and 100 s^{-1} in a rotational rheometer (**a**) and evolution with time of the pressure gradient in channel flow, at constant flow rate, for $Q = 1.37$, 2.95, 6.36, 13.6 and 29.5 µl/min (**b**) with the semi-dilute CTAB solution at $T = 22$ °C. Note that the flow rate in the microchannels is increased every 400 s and at the end the flow rate is reduced to the lowest value and the full sequence is repeated once again

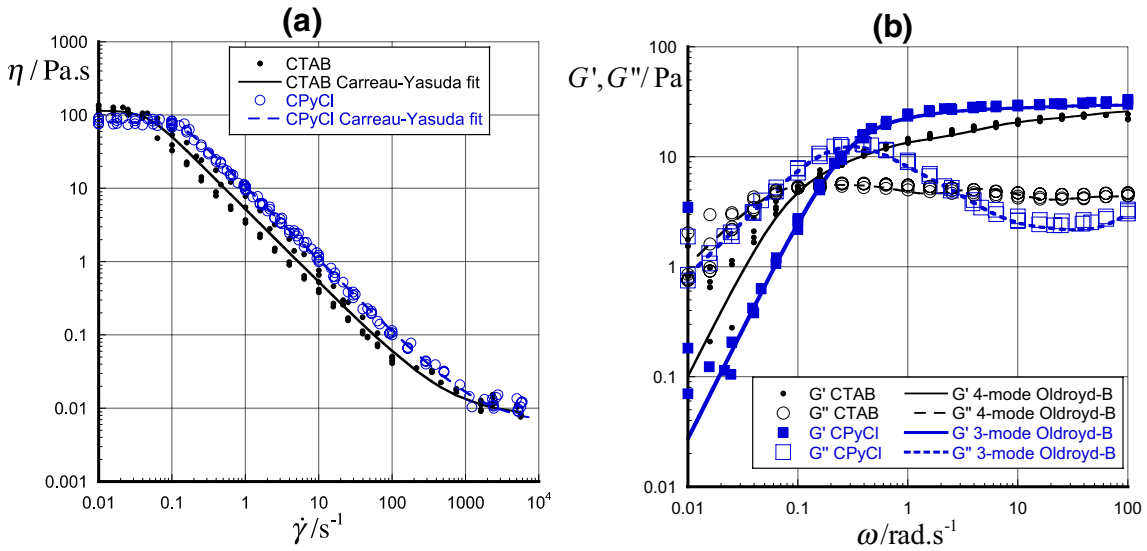

Fig. 6 Steady shear viscosity as a function of the shear rate (**a**) and storage and loss moduli measured in SAOS as a function of the angular frequency (**b**) for the semi-dilute solutions of CTAB and CPyCl at $T = 22$ °C. The Carreau–Yasuda model was fitted to the steady shear viscosity curves. Multimode Oldroyd-B models were fitted to the SAOS data

The Carreau–Yasuda model fitted to the semi-dilute CTAB solution viscosity data provided the following parameters: $\eta_\infty = 0.008$ Pa s; $\eta_0 = 115$ Pa s; $\Lambda = 22$ s; $n = 0.005$; $a = 3$. For the semi-dilute CPyCl solution the fitted coefficients were: $\eta_\infty = 0.006$ Pa s; $\eta_0 = 80$ Pa s; $\Lambda = 7.5$ s; $n = 0.005$; $a = 4$.

The linear rheology (SAOS measurements) complements the steady shear measurements by providing useful information about the wormlike micelles structure under conditions of small amplitude deformation. Figure 6b shows the G' and G'' curves of both semi-dilute solutions, and includes fittings by a 4-mode and a 3-mode Oldroyd-B model to the CTAB and CPyCl results, respectively. The model parameters for both fluids are listed in Table 1.

The results show many similarities between both storage moduli, with a better defined high frequency G' plateau for the CPyCl solution, whereas for the CTAB there is still a mild increase in G'. On the other hand, the G'' behavior of the CPyCl solution is very different from that of the CTAB solution and three different regions can be defined in the former spectrum: at low angular frequencies, G'' increases with ω as for CTAB, followed by a region at moderate frequencies in which G'' decreases and finally a nearly constant G'' is observed at high angular frequencies. The transition between the first and second regions ($\omega \approx 0.3$ rad/s) is marked by a maximum in G''. The differences between both semi-dilute solutions suggest that the CPyCl wormlike micelles are slightly more entangled than the CTAB wormlike micelles.

Following the characterization in shear, the extensional flow behavior of both solutions is reported next.

Figure 7 shows the time evolution of the normalized diameter of the thinning filaments for both semi-dilute solutions

Table 1 Relaxation times (λ_i) and viscosity coefficients (η_i) of the 4-mode (a) and 3-mode (b) Oldroyd-B models fitted to the response in SAOS of the semi-dilute CTAB and CPyCl solutions, respectively

i	1	2	3	4
(a)				
λ_i/s	11	2	0.2	0.02
η_i/Pa s	90	12.5	1.5	0.1
η_s/Pa s	0.02			

i	1	2	3
(b)			
λ_i/s	3.3	0.5	0.05
η_i/Pa s	80	2	0.1
η_s/Pa s	0.025		

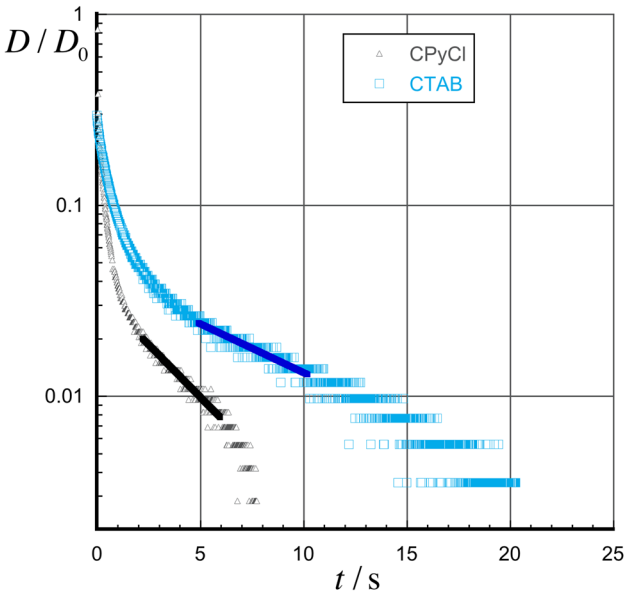

Fig. 7 Normalized diameter of the filament as a function of time measured in the CaBER device for the semi-dilute solutions of CPyCl and CTAB at $T = 22$ °C

using the CaBER rheometer. The experiments were repeated four times for each fluid to reduce the experimental uncertainty in the determination of the extensional relaxation time. Globally, the extensional relaxation time of the CTAB solution is higher than for the CPyCl solution. The extensional relaxation times obtained from averaging four experiments for each fluid are $\lambda_{\mathrm{CTAB}} = 2.9$ s and $\lambda_{\mathrm{CPyCl}} = 1.4$ s. These results suggest that under extensional flow the CTAB solution microstructures are more elastic than the CPyCl microstructures.

3.2 Flow visualizations

The experiments were carried out with the contraction channel described previously, at six different flow rates: $Q = 1.27$ µl/min, 2.12 µl/min, 4.25 µl/min, 8.49 µl/min, 21.2 µl/min and 42.5 µl/min. The shear rates for fully developed flows in a straight rectangular duct were calculated using the method described by Son (2007). Thus, the characteristic shear rates in the upstream/downstream channels and in the contraction channel are given by Eqs. (2) and (3) or (4), respectively (Son 2007),

$$\dot{\gamma}_{\mathrm{u}} = \left(\frac{6Q}{w_{\mathrm{u}}(h)^2}\right)\left(1 + \frac{h}{w_{\mathrm{u}}}\right) f^*\left(\frac{h}{w_{\mathrm{u}}}\right) \tag{2}$$

$$\dot{\gamma}_{\mathrm{c}} = \left(\frac{6Q}{w_{\mathrm{c}}(h)^2}\right)\left(1 + \frac{h}{w_{\mathrm{c}}}\right) f^*\left(\frac{h}{w_{\mathrm{c}}}\right) \quad \text{if } h \le w_{\mathrm{c}} \tag{3}$$

$$\dot{\gamma}_{\mathrm{c}} = \left(\frac{6Q}{h(w_{\mathrm{c}})^2}\right)\left(1 + \frac{w_{\mathrm{c}}}{h}\right) f^*\left(\frac{w_{\mathrm{c}}}{h}\right) \quad \text{if } h > w_{\mathrm{c}} \tag{4}$$

where w_{u} is the width of the upstream and downstream portions of the rectangular channel, w_{c} is the width of the contraction throat, h is the constant height of the channel, Q is the volumetric flow rate and $f^*(x)$ is the shape factor, given by (Son 2007):

$$f^*(x) = \left[\left(1 + \frac{1}{x}\right)^2\left(1 - \frac{192}{\pi^5 x}\sum_{i=1,3,5}^{\infty}\frac{\tanh\left(\frac{\pi}{2}ix\right)}{i^5}\right)\right]^{-1} \tag{5}$$

The Reynolds number (Re) quantifies the ratio between inertial and viscous effects. In a straight channel the definition of Re is fairly straightforward, but that is not the case for a contraction flow. Again, Re was calculated for fully developed channel flow in the upstream channel (Re_{u}) and in the contraction throat (Re_{c}), using the hydraulic diameter definition (White 1994):

$$Re_{\mathrm{u}} = \frac{\rho v_{\mathrm{u}} D_{h_u}}{\eta_{\mathrm{u}}} = \frac{\rho}{\eta_{\mathrm{u}}}\frac{Q}{w_{\mathrm{u}}h}\frac{2w_{\mathrm{u}}h}{(w_{\mathrm{u}} + h)} = \frac{2\rho Q}{\eta_{\mathrm{u}}(w_{\mathrm{u}} + h)} \tag{6}$$

$$Re_{\mathrm{c}} = \frac{\rho v_{\mathrm{c}} D_{h_c}}{\eta_{\mathrm{c}}} = \frac{\rho}{\eta_{\mathrm{c}}}\frac{Q}{w_{\mathrm{c}}h}\frac{2w_{\mathrm{c}}h}{(w_{\mathrm{c}} + h)} = \frac{2\rho Q}{\eta_{\mathrm{c}}(w_{\mathrm{c}} + h)} \tag{7}$$

where ρ is the fluid density, and η_{u} and η_{c} are the shear viscosities of the fluid calculated at the nominal shear rates in the upstream and at the contraction of the channel, respectively, i.e., for the characteristic shear rates given by Eqs. (2), (3), and (4).

The Elasticity number (El) can be calculated through the ratio between Wi and Re as $El_{\mathrm{u}} = Wi_{\mathrm{u}}/Re_{\mathrm{u}}$ and $El_{\mathrm{c}} = Wi_{\mathrm{c}}/Re_{\mathrm{c}}$, where Wi is the Weissenberg number. The Weissenberg number was calculated in the upstream (Wi_{u}) and contraction (Wi_{c}), respectively as

$$Wi_{\mathrm{u}} = \lambda_{\mathrm{CaBER}}\frac{\dot{r}_{\mathrm{u}}}{3} \tag{8}$$

$$Wi_{\mathrm{c}} = \lambda_{\mathrm{CaBER}}\frac{\dot{r}_{\mathrm{c}}}{3} \tag{9}$$

where λ_{CaBER} is the CaBER relaxation time.

The extension rate ($\dot{\varepsilon}$) was estimated as:

$$\dot{\varepsilon} = \frac{u_{\mathrm{c}} - u_{\mathrm{u}}}{w_{\mathrm{u}}} = \frac{Q}{w_{\mathrm{u}}h}\left(\frac{1}{w_{\mathrm{c}}} - \frac{1}{w_{\mathrm{u}}}\right) \tag{10}$$

while the Deborah number (De) was calculated as $De = \lambda_{\mathrm{CaBER}}\dot{\varepsilon}$.

3.2.1 Newtonian-like flow

The flow patterns obtained with a Newtonian fluid flowing through the 4:1:4 abrupt contraction for $Q = 42.5$ µl/min are symmetric and steady upstream and downstream of the contraction throat, and correspond to creeping flow conditions ($Re_u = 0.312$ and $Re_c = 0.804$). Experiments at lower flow rates with the Newtonian fluid also show similar flow dynamics, as expected.

Several experiments starting from the rest state were carried out up to a flow rate of $Q = 1.27$ µl/min with both semi-dilute surfactant solutions. The results obtained immediately after the start of the flow show the presence of an asymmetric flow with a long upstream jet bounded by two recirculation regions, as partially shown in Fig. 8a, which will be referred hereinafter as the transient asymmetric flow pattern.

After 20–30 min, the pathlines show that the flow has evolved to a new transient flow pattern with two bands with different velocities, as shown in Fig. 8b, which we designate hereinafter as transient shear-banding flow. Although this experiment was repeated several times, it was not possible to unequivocally clarify whether the transient flow patterns always change from the asymmetric to the shear-banding flow regime, but in almost all tests this change occurred at around 20–30 min after the onset of the flow from the rest state. Then, a second transition often takes place after a while, in which the flow finally becomes symmetric and Newtonian-like. However, as discussed below, the succession of flow states may differ. Again, it is also not totally clear when the flow becomes "Newtonian-like", because in some experiments, the transition to the established Newtonian-like flow regime took place after only a few minutes, while in others, the change occured after almost 30 min. Unlike the asymmetric and shear-banding flow patterns that are transient, the visualizations suggest that the Newtonian-like flow pattern (Fig. 8c) is stable over time, even for experiments carried out for more than 1 h. The visualizations, in particular those for experiments carried out for a long period of time, show sometimes the absence of one of the transient regimes, but the established Newtonian-like flow pattern was always observed for this range of flow rates.

The flow rate was further increased to $Q = 2.12$ µl/min to assess its influence on the flow patterns. This was done in two different ways, leading also to distinct results. If we start from the stabilized Newtonian-like flow at $Q = 1.27$ µl/min, and then suddenly increase the flow rate to $Q = 2.12$ µl/min, the flow patterns remain unchanged and Newtonian-like for the whole duration of the process. If instead the experiment at $Q = 2.12$ µl/min is started from a rest state, then we observe a similar behavior to that seen previously for $Q = 1.27$ µl/min, except that the transitions between the various flow patterns take place faster than with the experiment at $Q = 1.27$ µl/min. As seen at the lower flow rate, the experiments at $Q = 2.12$ µl/min may show the absence of one of the intermediate transient flow regimes.

Experiments carried out with a different contraction ratio and hyperbolic contraction, as well as with variations on the different channel aspect ratios (all geometries of Figs. 3 and 4), show that they have negligible influence on the Newtonian-like flow regime exhibited by both semi-dilute surfactant solutions.

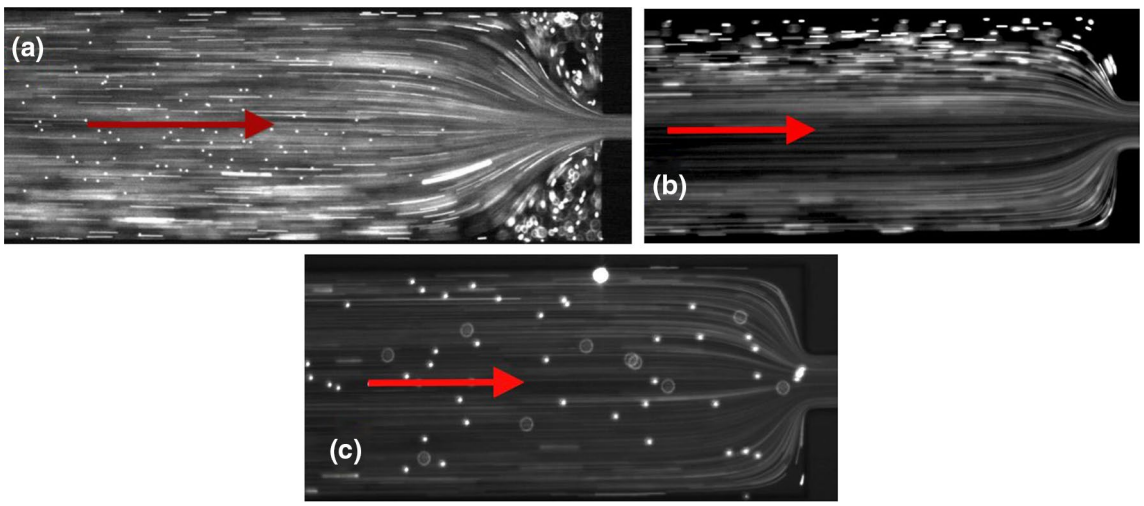

Fig. 8 Flow patterns in the 4:1:4 abrupt contraction (400 µm × 100 µm channel) for $Q = 1.27$ µl/min ($\dot{\gamma}_u = 36.8\ s^{-1}$, $Re_u = 5.70 \times 10^{-4}$, $Wi_u = 35.4$, $\dot{\gamma}_c = 187\ s^{-1}$, $Re_c = 6.12 \times 10^{-3}$ and $Wi_c = 180$) with the semi-dilute CTAB solution at $T = 22$ °C starting from the rest state. **a** Transient asymmetric flow pattern after 5 min; **b** transient shear-banding flow field after 20 min; **c** established Newtonian-like flow pattern

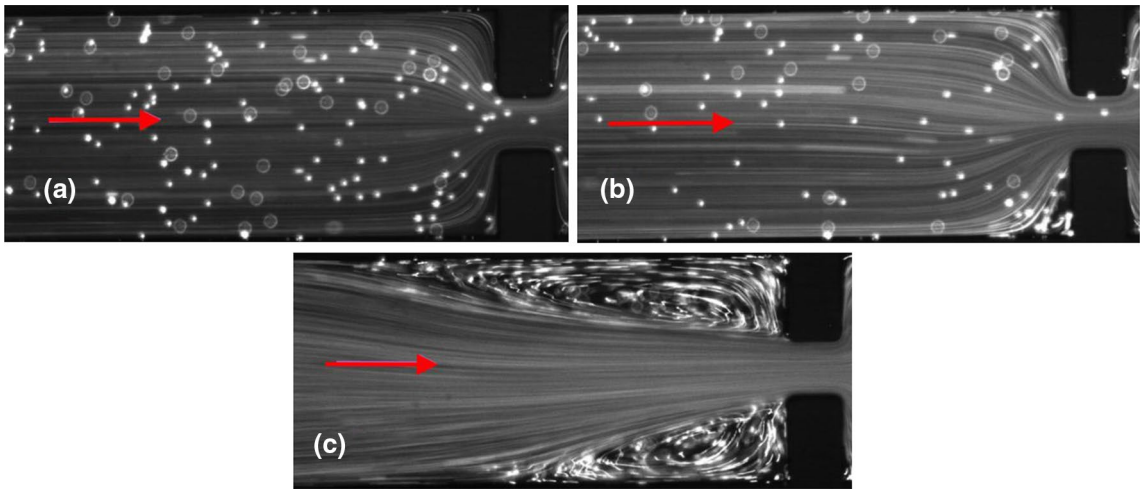

Fig. 9 Evolution with time of the asymmetric flow field for $Q = 4.25$ µl/min ($\dot{\gamma}_u = 123\,s^{-1}$, $Re_u = 5.66 \times 10^{-3}$, $Wi_u = 118$, $\dot{\gamma}_c = 627\,s^{-1}$, $Re_c = 0.0454$ and $Wi_c = 602$) from an established Newtonian-like flow pattern corresponding to a flow rate $Q = 2.12$ µl/min for the semi-dilute CTAB solution. **a** Just after the increase of flow rate (established Newtonian-like flow pattern); **b** 5 min after the increase of flow rate; **c** 20 min after the increase of flow rate (established asymmetric flow pattern)

3.2.2 Asymmetric flow

For higher flow rates, between $Q = 4.25$ and 21.2 µl/min, the established flow patterns correspond to an asymmetric flow regime. Unlike with the Newtonian-like flow pattern, the progression to the established asymmetric flow regime is fast and shows almost no intermediate state in experiments starting from rest. However, in the experiments starting from a lower flow rate, pertaining to the stabilized Newtonian-like flow regime, the transient of the intermediate states is long lived, as shown in Fig. 9.

The established asymmetric flow pattern is characterized by an asymmetric central jet and two asymmetric separated flow regions at the upstream contraction corners, as shown in Fig. 9c. The observed jetting behavior is reminiscent of earlier observations by Ober et al. (2013), Haward et al. (2014) and Salipante et al. (2017, 2018) in rectangular flows. Experiments lasting longer than 1 h suggest that the asymmetry changes randomly with time, whereas other experiments show that the lengths of the upstream jet and upstream vortices increase with the flow rate. The vortex length and, particularly, the flow asymmetry are much more pronounced in high contraction ratio channels, but the overall flow features are qualitatively similar. The contraction shape also has a strong influence on the flow patterns in the asymmetric flow regime, but slightly different types of behavior are observed for the semi-dilute CTAB and CPyCl solutions. For the semi-dilute CTAB solution, the flow asymmetry is stronger in the abrupt contractions than in the corresponding hyperbolic contractions. In contrast, the semi-dilute CPyCl solution shows sometimes the opposite behavior, as depicted in Fig. 10, where for geometries C1 and HC1, the established asymmetric flow pattern is more asymmetric in flows through the hyperbolic contraction than through the corresponding abrupt contraction. On the other hand, in experiments carried out with the HC2 hyperbolic contraction and the corresponding C2 abrupt contraction at $Q = 8.49$ µl/min, the asymmetry is stronger in the abrupt contraction than through its hyperbolic sibling, as observed for the

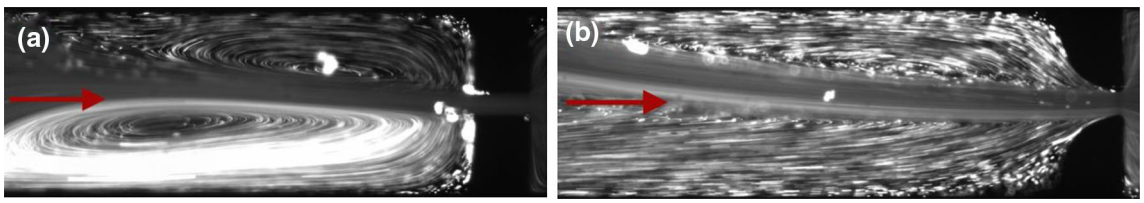

Fig. 10 Influence of the contraction shape on the established asymmetric flow pattern for experiments carried out with the semi-dilute CPyCl solution for $Q = 8.49$ µl/min. **a** C1 abrupt contraction ($\dot{\gamma}_u = 257\,s^{-1}$, $Re_u = 0.012$, $Wi_u = 119$, $\dot{\gamma}_c = 3780\,s^{-1}$, $Re_c = 0.22$ and $Wi_c = 1750$); **b** HC1 hyperbolic contraction ($\dot{\gamma}_u = 257\,s^{-1}$, $Re_u = 0.012$, $Wi_u = 119$, $\dot{\gamma}_c = 3480\,s^{-1}$, $Re_c = 0.22$ and $Wi_c = 1610$)

semi-dilute CTAB solution. Since the history of deformation is different along both types of contraction, with the flow through the hyperbolic contraction exhibiting a more homogeneous extensional rate, and higher Weissenberg numbers, while Reynolds numbers remain small, elastic behavior is expected to be the dominant influence on this flow regime.

The channel aspect ratio also plays a non-negligible role on the established asymmetric flow regime. In this case, the results suggest that the flow instabilities, assessed by the length and asymmetry of the jet, increase with the channel aspect ratio.

3.2.3 Disordered flow

This flow regime is characterized by a chaotic-like flow field, or at least a disordered flow, as Fig. 11 illustrates, where we can see a disturbed upstream flow, slightly asymmetric, with two small recirculations at the upstream corners. Whereas the asymmetric flow maintained characteristics of an organized steady flow for long periods of time, before switching to a new asymmetric flow configuration, the disordered flow is continuously varying in time.

The disordered flow regime differs from the two previously described flow patterns (Newtonian-like and asymmetric flow fields), but is arrived at from any of both by increasing the flow rate. In all situations, the transition to this regime takes place over a period of time of less than 1 min, thus the transient between those two lower flow rate regimes and this regime will not be analyzed. The disordered flow regime also shares many similarities with the unstable flow observed by Haward et al. (2012) and Dubash et al. (2012) in surfactant flows through cross-slot devices.

It is clear from the experiments that the contraction ratio and shape influence the disordered flow patterns. An increase in the contraction ratio enhances flow instabilities in the disordered flow regime, and similarly using an abrupt contraction in comparison with the use of an hyperbolic contraction also enhances the instabilities, presumably because of the less homogeneous flow kinematics of the former.

The effect of the channel aspect ratio is less pronounced, but the data still suggest that the flow instabilities for flows in the disordered flow regime increase with the channel aspect ratio.

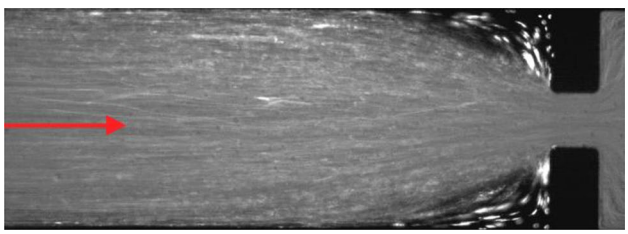

Fig. 11 Illustration of a disordered flow pattern

3.2.4 Flow transitions

This section discusses the flow transitions between the established flows described previously. It is important to refer that it is difficult to delineate clearly the flow transitions, because of their wide variability between different experiments, to which the time dependency of the rheology of the surfactant solutions is certainly not a stranger. In what follows, the transition between the Newtonian-like and asymmetric flow regimes will be designated as the first flow transition and the flow transition from the asymmetric to the disordered flow regime will be denoted as the second flow transition. A third transition can be found when the flow is increased from the Newtonian-like regime directly to the disordered flow regime, but here we will only analyze the first two transitions (just mentioned).

The experiments suggest that to properly describe the flow transitions, both the dimensions of the channel and the dimensions of the contraction should be taken into account. Despite some particular differences between the fluid dynamics of both semi-dilute surfactant solutions, such as the different behavior of the established asymmetric flow pattern under changes of contraction shape, the overall behavior is similar.

The dimensionless numbers used to characterize the flow are calculated considering the shear rate at the wall, but the micellar structures experience a wide range of shear rates from zero on the centerline to the maximum wall values. Therefore, the following flow maps are not aimed at establishing a direct link between the flow transitions and the behavior of the wormlike micelles, but to provide a method to predict the flow behavior considering the flow rate and the overall dimensions of the microchannel.

Figure 12 shows that the Elasticity number–Deborah number parameter space maps are able to characterize both flow transitions for both semi-dilute surfactant solutions in all types of contractions. These two dimensionless numbers are based on the dimensions of the channel and of the contraction, thus they are both unaffected by the contraction shape. The Deborah number is related to the relaxation mechanism of the wormlike micelles and with the extension rate experienced by the fluid elements in the contraction region. On the other hand, the Elasticity number in the contractions is defined as the ratio between elastic and inertial effects in the contraction throat. There are some inconsistencies, in the sense that some flow patterns overlap near the transition curves, which is also the consequence of the nature of the experiments, and of the difficulty to define the beginning and the end of the established flow regimes over the whole range of flow rates and of starting conditions

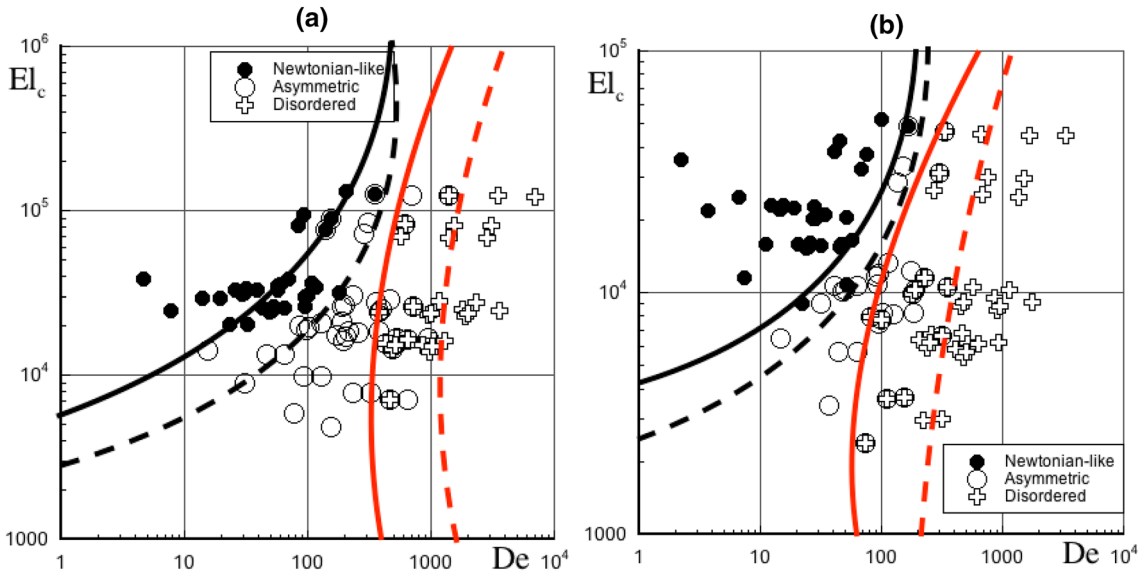

Fig. 12 Map identifying the established Newtonian-like, asymmetric and disordered flow regimes as a function of the Deborah number and the Elasticity number in the contraction for experiments carried out with the semi-dilute CTAB solution (**a**) and with the semi-dilute CPyCl solution (**b**). Lines were sketched to tentatively separate the various types of flow, with the black solid line and the black dashed line marking the start and the end of the first flow transition, whereas the red solid line and the red dashed lines mark the start and the end of the second flow transition

tested. However, overall, the flow regimes can be identified in the illustrated parameter space maps. The data suggest that both transitions depend simultaneously on both *De* and El_c, but the second flow transition is less dependent on El_c than the first one. On the other hand, the transitions take place at high values of El_c and *De*, which suggest that the relevant dimensionless numbers ought to be different ones.

3.2.5 Particle velocimetry in the asymmetric and disordered flow regimes

The asymmetric and disordered flow patterns and the second flow transition were further investigated, through the analysis of the μPIV results. The visualizations in the asymmetric and disordered flow regimes suggest that the streamwise velocity should oscillate at the interface between the jet and the separation vortices, with the jet asymmetry changing over time from one side of the channel to the other. The flow visualizations indicate that this change is non-periodic and relatively slow in the asymmetric flow regime, thus further experiments were carried out to the measure the velocity field with a μPIV system at acquisition frequencies between 0.5 and 5 Hz, whereas the fast μPIV was used in experiments in the disordered flow regime at frequencies of acquisition between 500 and 1000 Hz. Figure 13 shows the map with the locations, where the streamwise velocity component (u) was measured.

Figure 14a plots the time series of the streamwise velocity component (u) at the three locations A, B and C illustrated

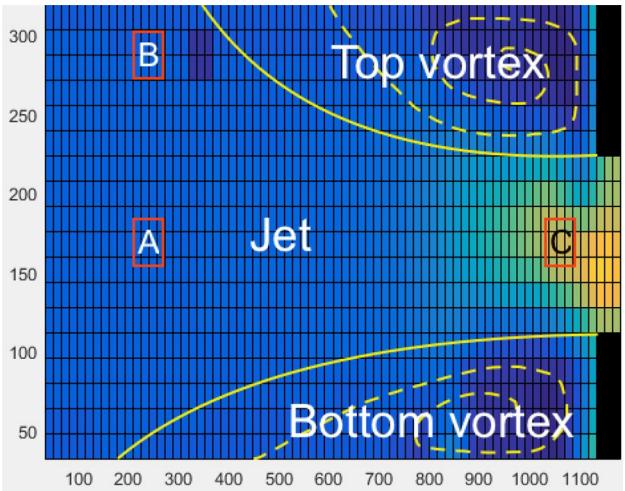

Fig. 13 Illustration of the locations where the variation with time of the streamwise velocity (u) was monitored (flow from left to right): central plane in the upstream channel (A); interface between the jet and the upper separation vortex (B); central plane at the contraction (C). The experiments were carried out with the normal μPIV at 1 Hz using the 8:1:8 abrupt contraction channel ($h = 100$ μm) for $Q = 4.25$ μl/min

in Fig. 13, acquired at a frequency of 1 Hz for $Q = 4.25$ μl/min (asymmetric flow regime) in the 8:1:8 abrupt contraction ($h = 100$ μm). This experiment was carried out for more than 20 min, but here the behavior of the streamwise velocity component (u) is plotted only for 1 min. The small fluctuations in the velocity field (u) show that the asymmetric flow

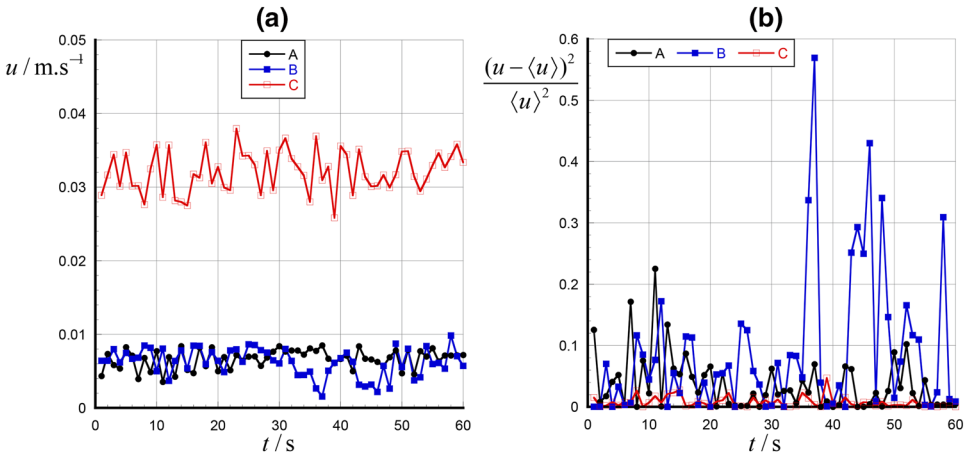

Fig. 14 Time evolution of the streamwise velocity component (**a**) and normalized quadratic difference between the instantaneous local streamwise velocity and the corresponding time average (**b**) at locations A, B and C (see Fig. 13) for an experiment carried out with the normal μPIV at $f=1$ Hz using the 8:1:8 abrupt contraction channel ($h=100$ μm) for $Q=4.25$ μl/min with the semi-dilute CTAB solution

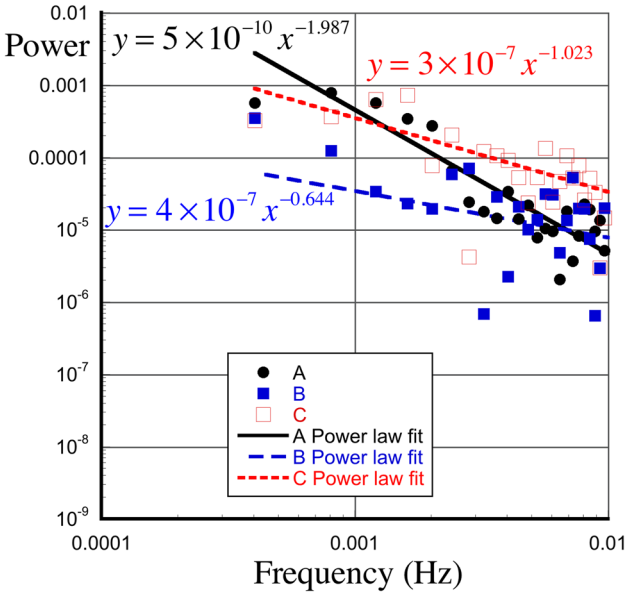

Fig. 15 Power spectra of the streamwise velocity at locations A, B and C for the flow of a semi-dilute CTAB solution in the 8:1:8 abrupt contraction with $h=100$ μm and $Q=4.25$ μl/min. Data obtained with the normal μPIV at $f=1$ Hz

is locally unstable. As expected, the velocity in the central plane at the contraction throat (location C) is clearly higher than elsewhere in the upstream channel (locations A and B), but not if cast in terms of a normalized fluctuation, as in Fig. 14b. Indeed, the velocities in the upstream center plane (locations A and C) also oscillate slightly less (in relative terms) than at the offset point (B), as better shown in Fig. 14b.

The power spectra computed using the fast Fourier Transform (FFT) of the velocity time series at each location (A, B and C), for experiments carried out for more than 20 min, show negative slopes in log–log coordinates, as plotted in Fig. 15, indicative of a power law decay with f. The slopes vary between − 0.64 and − 1.99 and are lower in magnitude than those expected for elastic turbulence (slopes between − 3 and − 4) (Jun and Steinberg 2009), thus excluding this behavior at these flow conditions. The magnitude of the slope is higher in point A than at the other two locations.

The experiments in the disordered flow regime showed very fast variations (of the order of milliseconds) of the asymmetry of the jet and of the boundaries of the separated flows regions. As observed in the data for the asymmetric flow regime, the power spectra slopes in log–log coordinates are negative and with a magnitude of around 1, so again not corresponding to the elastic turbulence regime; therefore, they are not shown here for conciseness.

All μPIV measurements, carried out with both semi-dilute surfactant solutions, suggest that the asymmetric and the disordered flow patterns are globally stable, but the flow characteristics are locally unstable. The power spectra slopes do not clarify the origin of these local instabilities, but considering the wormlike micellar structure of the semi-dilute solutions, they can be the outcome of the local alignment of the wormlike micelles and of the interaction between bands with aligned and non-aligned structures. Therefore, considering these results, it is fair to conclude that the mechanism behind the local instabilities of both semi-dilute solutions should be of the same type.

Finally, it is important to refer that we could not find characteristic frequencies associated with the fluctuations in these two flow regimes, as has been found in flows around a cylinder in a micro-channel by Dey et al. (2018) and more recently by Haward et al. (2019).

4 Conclusions

Experiments on the flow of semi-dilute solutions of CTAB and CPyCl through micro-channels, incorporating abrupt and hyperbolic contractions, were carried out to investigate

the flow characteristics as well as the type and nature of the observed flow instabilities. The flow conditions tested are characterized by Reynolds numbers below 1.

The rheological measurements showed that the semi-dilute surfactant solutions are strongly shear-thinning, in particular exhibiting a constant shear stress over a wide range of shear rates, an indication of shear banding, and with low and high shear rate plateaus of constant viscosity. They also showed a viscoelastic behavior in SAOS flow measurements and a high extensional relaxation time in the CaBER experiments.

The flows of the semi-dilute solutions through the microchannels exhibited a complex behavior with three established flow regimes and in some cases rather long-lived transient processes between them. The three established flow regimes were denoted as Newtonian-like, asymmetric and disordered flow.

Newtonian-like flows occurred at low flow rates and were preceded by a long transient regime in experiments carried out from the rest state. Haward and McKinley (2012) and Dubash et al. (2012) also reported a similar Newtonian-like flow regime in microfluidic cross-slot flows, but in contrast the experiments carried out by Lutz-Bueno et al. (2015) in mini-scale slit channels did not show Newtonian-like flow patterns at low flow rates.

The asymmetric flow regime seems to be the outcome of, or at least it is related to, the dynamics of the entangled wormlike micelles. The experiments starting from a condition pertaining to an established Newtonian-like flow showed a long transient process before setting on the established asymmetric flow pattern, whereas the experiments from the rest state showed a fast transient process to the established asymmetric flow, which vanished within less than 1 min from the beginning of the experiment.

The flow visualizations suggest that the disordered flow regime is chaotic-like and the μPIV measurements showed that both the asymmetric and the disordered flow patterns share similarities, even though the oscillation of the jet asymmetry is much faster in the disordered flow regime (characteristic time of the order of milliseconds) than in the asymmetric flow regime (of the order of seconds). Therefore, the transition between both flow regimes is characterized by a sudden increase of the frequency of oscillation of the upstream channel flow asymmetry. The disordered flow regime seems to be related to the breakdown of the entangled wormlike micelles, but this hypothesis should be considered with caution, because the fluid mechanics literature is abundant in cases in which there is a flow transition without the concomitant transition in the fluid microstructure, so further investigation is needed to clarify this issue. The slope of the power spectra of the velocity fluctuations in these flow regimes were comprised between − 0.5 and − 2, so well below the characteristic slopes of the elastic turbulence. The disordered flow patterns showed similarities to the unstable bifurcated flow reported by Haward and McKinley (2012) and Dubash et al. (2012) in complex microfluidic cross-slot flows.

Acknowledgements All authors acknowledge funding by Centro de Estudos de Fenómenos de Transporte (CEFT) and Fundação para a Ciência e a Tecnologia (FCT) via projects UID/EMS/00532/2013 and UID/EMS/00532/2019. R. Matos is also indebted to FCT for the PhD scholarship SFRH/BD/86029/2012.

References

Berret JF (2005) Rheology of wormlike micelles : equilibrium properties and shear banding transition. In: Weiss RG, Terech P (eds) Molecular gels. Springer, Berlin, pp 235–275. https://doi.org/10.1007/1-4020-3689-2_20

Bewersdorff HW, Frings B, Lindner P, Oberthür RC (1986) The conformation of drag reducing micelles from small-angle-neutron-scattering experiments. Rheol Acta 25:642–646. https://doi.org/10.1007/BF01358173

Dey AA, Modarres-Sadeghi Y, Rothstein JP (2018) Viscoelastic fluid-structure interactions between a flexible cylinder and wormlike micelle solution. Phys Rev Fluids 3:063301. https://doi.org/10.1103/PhysRevFluids.3.063301

Dubash N, Cheung P, Shen AQ (2012) Elastic instabilities in a microfluidic cross-slot flow of wormlike micellar solutions. Soft Matter 8:5847. https://doi.org/10.1039/c2sm25215e

Groisman A, Steinberg V (2000) Elastic turbulence in a polymer solution flow. Nature 405(6782):53–55. https://doi.org/10.1038/35011019

Haward SJ, McKinley GH (2012) Stagnation point flow of wormlike micellar solutions in a microfluidic cross-slot device: Effects of surfactant concentration and ionic environment. Phys Rev E Stat Nonlinear Soft Matter Phys 85:1–14. https://doi.org/10.1103/PhysRevE.85.031502

Haward SJ, Ober TJ, Oliveira MSN, Alves MA, McKinley GH (2012) Extensional rheology and elastic instabilities of a wormlike micellar solution in a microfluidic cross-slot device. Soft Matter 8:536. https://doi.org/10.1039/c1sm06494k

Haward SJ, Galindo-Rosales FJ, Ballesta P, Alves MM (2014) Spatiotemporal flow instabilities of wormlike micellar solutions in rectangular microchannels. Appl Phys Lett 104(12):124101. https://doi.org/10.1063/1.4869476

Haward SJ, Kitajima N, Toda-Peters K, Takahashi T, Shen AQ (2019) Flow of wormlike micellar solutions around microfluidic cylinders with high aspect ratio. Soft Matter 15(9):1893–2104. https://doi.org/10.1039/c8sm02099j

Holmberg K, Jönsson B, Kronberg B, Lindman B (1998) Surfactants and polymers in aqueous solutions. IEEE Electr Insul Mag 14(5):42–43. https://doi.org/10.1109/mei.1998.714652

Hu YT, Boltenhagen P, Pine DJ (1998) Shear thickening in low-concentration solutions of wormlike micelles. I. Direct visualization of transient behavior and phase transitions. J Rheol 42:1185. https://doi.org/10.1122/1.550926

Jun Y, Steinberg V (2009) Power and pressure fluctuations in elastic turbulence over a wide range of polymer concentrations. Phys Rev Lett 102:124503. https://doi.org/10.1103/physrevlett.102.124503

Kawaguchi Y, Segawa T, Feng Z, Li P (2002) Experimental study on drag-reducing channel flow with surfactant additives-Spatial structure of turbulence investigated by PIV system. Int J Heat Fluid Flow 23:700–709. https://doi.org/10.1016/S0142-727X(02)00166-2

Kim NJ, Pipe CJ, Ahn KH, Lee SJ, McKinley GH (2010) Capillary breakup extensional rheometry of a wormlike micellar solution. Kor Aust Rheol J 22(1):31–41

Koskie JE, Tiederman WG (1991) Turbulence structure and polymer drag reduction in adverse pressure gradient boundary layers. Internal report of Purdue University for Office of Naval Research, PME-FM-91-3

Lopez-Diaz D, Sarmiento-Gomes E, Garza C, Castillo R (2010) A rheological study in the dilute regime of the worm-micelle fluid made of zwitterionic surfactant (TDPS), anionic surfactant (SDS), and brine. J Coll Interface Sci 348(1):152–158. https://doi.org/10.1016/j.jcis.2010.03.038

Lutz-Bueno V, Kohlbrecher J, Fischer P (2015) Micellar solutions in contraction slit-flow: alignment mapped by SANS. J Non-Newton Fluid Mech 215:8–18. https://doi.org/10.1016/j.jnnfm.2014.10.010

Manero O, Bautista F, Puig JE (2010) Rheology of surfactants: wormlike micelles and lamellar liquid crystalline phases. Rheology II:17

Ober T, Haward SJ, Pipe CJ, Soulages J, McKinley GH (2013) Microfluidic extensional rheometry using a hyperbolic contraction geometry. Rheol Acta 52(6):529–546. https://doi.org/10.1007/s00397-013-0701-y

Povkh IL, Stupin AB, Maksjutenko SN, Aslanov PV, Roshchin EA, Tur AN (1975) 'Study of the turbulent flow of solutions of surface active materials by means of a laser anemometer (in Russian). Inzhenerni-Fizicheskii Zhurnal 29:853–856

Puig JE, Escalante JI, Soltero JFA, Bautista F, Manero O (2012) Rheological behavior of dilute micellar solutions. In: Somasundaran P (ed) Encyclopedia of surface and colloid science, 2nd edn. Taylor and Francis, New York

Rehage H, Hoffmann H (1988) Rheological properties of viscoelastic surfactant systems. J Phys Chem 92(16):4712–4719. https://doi.org/10.1021/100327a031

Salipante PF, Little CAE, Hudson SD (2017) jetting of a shear banding fluid in rectangular ducts. Phys Rev Fluids 2(3):033302. https://doi.org/10.1103/PhysRevFluids.2.033302

Salipante PF, Meek SE, Hudson SD (2018) Flow fluctuations in wormlike micelle fluids: Soft matter. R Soc Chem 14(44):9020–9035. https://doi.org/10.1039/C8SM01649F

Savins JG (1967) A stress-controlled drag-reduction phenomenon. Rheol Acta 6:323–330. https://doi.org/10.1007/BF01984629

Son Y (2007) Determination of shear viscosity and shear rate from pressure drop and flow rate relationship in a rectangular channel. Polymer 48:632–637. https://doi.org/10.1016/j.polymer.2006.11.048

Sood AK, Bandyopadhyay R, Basappa G (1999) Linear and nonlinear rheology of wormlike micelles. Pramana J Phys 53(1):223–235. https://doi.org/10.1007/s12043-999-0151-3

White FM (1994) Fluid mechanics, 6th edn. McGraw-Hill, New York

Zakin JL, Ge W (2010) Polymer and surfactant drag reduction in turbulent flows. Polym Phys Suspens Nanocomposites Beyond 5:89–127. https://doi.org/10.1002/9780470600160.ch2